Empirical and Computational-Based Phase Predictions of Thermal Sprayed High-Entropy Alloys

Ecio Bosi[1] · Ashok Meghwal[1] · Surinder Singh[1] · Paul Munroe[2] · Christopher C. Berndt[1] · Andrew Siao Ming Ang[1]

Abstract Due to the wide range of compositional possibilities in the high-entropy alloy (HEA) field, empirical models and the CALPHAD method have been implemented to efficiently design HEAs. Although most design strategies have been tested on as-cast alloys, their validation for thermal sprayed HEA coatings is lacking. In this work, empirical models and the CALPHAD method under equilibrium and non-equilibrium conditions are assessed for phase prediction in five HEAs in the as-cast, laser clad and thermal sprayed conditions. High-velocity oxygen fuel coatings were prepared for these five HEAs, and their phases were identified by the x-ray diffraction analysis. These processes, even though their cooling rates vary significantly, show similar phase formation as indicated by a literature review and the current experimental study. The CALPHAD equilibrium calculation predicted most of the phases at specified temperatures. Furthermore, the CALPHAD-based non-equilibrium simulations correctly predicted the major phases present in the HEA coatings. The empirical models also show good prediction capability, but the intermetallic sigma phase is problematic for the parameter-based models. Therefore, the CALPHAD method can be used to efficiently design and develop HEAs prepared under conditions that encompass rapid cooling, such as occurring during thermal spray processes.

Introduction

Based on compositional principles, high-entropy alloys (HEAs) are composed of five or more elements with each varying between 5 and 35% in atomic percentage. On the other hand, based on entropy considerations, HEAs are categorized with a configurational entropy higher than or equal to 1.5R, where R is the ideal gas constant (Ref 1, 2). The high configurational entropy associated with HEAs promotes solid solution formation and decreases intermetallic phase stability, thereby reducing the number of phases formed (Ref 3). Furthermore, the HEA design concept shifts the focus from the boundaries of a multi-component phase diagram, usually studied in conventional alloys, to the unexplored central regions of quinary, senary, septenary, etc., compositional space (Ref 2, 4).

As-cast HEAs can achieve superior properties than conventional materials, including higher strength, hardness and excellent wear, corrosion, and oxidation resistance (Ref 5-7). More importantly, the notable properties of HEAs can be exploited in the form of surface coatings via methods such as thermal spray, laser cladding and vapor deposition. Thermal spray (TS), with its wide manufacturing scale and flexibility to support various feedstock forms, offers the potential to develop high-entropy alloy coatings for extreme engineering environments. This is important in the development of HEAs since the characteristics of HEAs may vary profoundly according to their

✉ Andrew Siao Ming Ang
aang@swin.edu.au

[1] Faculty of Science, Engineering and Technology, Department of Mechanical Engineering and Product Design Engineering, Australian Research Council (ARC) Industrial Transformation Training Centre in Surface Engineering for Advanced Materials (SEAM), Swinburne University of Technology, H38, P.O. Box 218, Hawthorn, VIC 3122, Australia

[2] School of Materials Science and Engineering, University of New South Wales, Sydney, NSW 2052, Australia

composition. Reports of TS HEA coatings surpassing traditional materials have stimulated research in this field (Ref 8).

The main motivation in HEA studies relies on the concept that a high configurational entropy favors a single-phase solid solution (SSS) over intermetallic compounds (IM) (Ref 2, 9, 10). However, studies have indicated that the phase formation in HEAs cannot be entirely justified by the stability rule based on configurational entropy (Ref 11, 12). According to Steurer (Ref 13), only 20% of HEAs were composed of SSS, based on data extracted from over 3100 papers on HEAs published up to 2019. This literature survey indicated that the random selection of elements does not always lead to HEAs with single-phase solid solutions.

Due to the availability of a vast compositional hyperspace, researchers have implemented strategies such as empirical models (Ref 14-27) and the CALPHAD method (Ref 28-30) to efficiently design HEAs. Within the domain of empirical models, parameter-based models were developed to predict phase formation and stability in HEAs (Ref 31). The parameters compare the chemical and topological similarity between the elements in an alloy, functioning as extensions of Hume-Rothery's solid solubility rules (Ref 17, 32). The most used parameter for chemical comparison is the mixing enthalpy (ΔH_{mix}), while the atomic size difference (δ) often represents topological similarity; i.e., the more similar the elements, the higher the alloy's tendency to form solid solutions. The criteria for solid solution phase formation are obtained by plotting the parameter values for reported alloys, correlating these with the phases found in the literature and delineating the regions corresponding to solid solutions (Ref 33).

Another strategy for predicting phase formation is the free energy-based models, which compare the driving forces for forming solid solutions and intermetallic phases (Ref 33). The major difference between the free energy-based models is the hypothetical intermetallic compound that competes for solute in the solid solution (Ref 23). Li et al. (Ref 33) benchmarked the accuracies of parameter-based and free energy-based models with the data available in the open literature and concluded that the free energy-based models more reliably predicted phase formation than parameter-based models.

The processing route plays a significant role in using empirical models for phase prediction. The most common method for synthesizing HEAs is the melting and casting route, either by vacuum arc melting or vacuum induction melting (Ref 34). Therefore, most of the experimental data are derived from materials in the as-cast condition. Since the empirical models depend on experimental results to determine their criteria values, they may not be effective for processes with higher cooling rates than casting, such as thermal spraying and laser cladding.

Another method for predicting solid solution phases is the computational approach based on CALPHAD. The principle of the CALPHAD method is to use thermodynamic models for fitting experimental data from binary and ternary phase diagrams, thereby allowing extrapolation for higher-order alloys (Ref 4). Thus, a reliable database with as many assessed phase diagrams for the studied system is crucial for accurate predictions using CALPHAD (Ref 35, 36). This is true for conventional materials, such as steels, which have a large set of available experimental data. However, HEAs are new materials that follow from unconventional alloy design strategy. Thus, the availability of a dedicated HEA database and its accuracy and reliability for phase prediction is limited and still under development. Recently, engineering software packages, such as Thermo-Calc (Ref 37) and Pandat (Ref 38), released their HEA databases, called TCHEA and PAN-HEA, respectively.

Equilibrium phase diagrams assume infinite slow cooling so that equilibrium is reached at every step of solidification. However, for non-equilibrium processing routes, such as thermal spraying, the rapid cooling rates do not allow the equilibrium redistribution of alloying elements (Ref 34). Consequently, Thermo-Calc and Pandat simulate solidification by the Scheil model, which employs the Scheil-Gulliver equation (Ref 39) and its derivatives. These equations consider reduced or negligible diffusion in the solidified structure, resulting in a more accurate estimation of the phases before any subsequent heat treatment (Ref 40).

In this work, both empirical models and the CALPHAD method simulate phase formation for HEA compositions: $CoCrFeNi$,[1] $CoCrFeNiMo_{0.2}$, $CoCrFeNiMo_{0.5}$, AlCrFeMnNi and AlCoCrFeNi. The alloy CoCrFeNi is not considered a HEA, since it has only four elements and its configurational entropy is lower than 1.5R. Nevertheless, this composition is investigated in this paper since it is reported in many studies. Co, Cr, Fe and Ni were selected as the primary elements for investigation as they are the most used elements in HEA coatings, followed by Al (Ref 8, 41). The study also includes Mo as an element that promotes intermetallic compound formation (Ref 42) and Mn in a Co-free composition. Since the CALPHAD and empirical approaches depend on databases, it is important to examine their accuracy with less frequently employed elements, such as Mo and Mn.

---

[1] Equimolar quaternary alloys, such as CoCrFeNi, are defined as medium entropy alloys (MEAs). MEAs are categorized with a configurational entropy (ΔS_{mix}) higher than or equal to 1.0R and lower than 1.5R (Ref 78). However, to ensure consistency with prior research and open literature, the widely used term "HEA" is employed for CoCrFeNi in this study.

Table 1 The parameter and free energy-based models and their respective solid solution forming criteria to assess high-entropy alloy phase prediction using empirical approaches. Number of citations on the Scopus database (until September 2022)

Model	Author	Solid solution criteria		Number of citations
M1	Zhang et al. (Ref 14)	$-15 \leq \Delta H_{mix} \leq 5$ kJ/mol		1537
		$12 \leq \Delta S_{mix} \leq 17.5$ J/K.mol		
		$\delta \leq 4.6\%$		
M2	Yang et al. (Ref 16)	$\Omega = \frac{T_m \Delta S_{mix}}{|\Delta H_{mix}|} \geq 1.1$		1222
		$\delta \leq 6.6\%$		
M3	Guo et al. (Ref 15)	$-22 \leq \Delta H_{mix} \leq 7$ kJ/mol		1099
		$11 \leq \Delta S_{mix} \leq 19.5$ J/K mol		
		$\delta \leq 8.5\%$		
M4	Ye et al. (Ref 22)	$0 < \delta < 5\%$		1043
		$-15 < \Delta H_{mix} < 5$ kJ/mol		
M5	Andreoli et al. (Ref 26)	BCC	FCC	24
		$3.59 \leq \Delta H_{el} \leq 20.08$ kJ/mol	$\Delta H_{el} \leq 6.8$ kJ/mol	
		$4.0 \leq VEC \leq 6.2$	$VEC \geq 8.0$	
M6	Jiang et al. (Ref 27)	BCC	FCC	28
		$-7.27 < \Delta H_{mix} < 4$ kJ/mol	$-7.27 < \Delta H_{mix} < 4$ kJ/mol	
		$\delta < 4.27\%$	$\delta < 4.27\%$	
		$VEC < 6.87$	$VEC > 8$	
M7	Troparevsky et al. (Ref 23)	$-T_{ann}\Delta S_{mix} < \Delta H_f < 37$ meV/atom		291
M8	Senkov et al. (Ref 24)	$k_1 < k_1^{cr}$		131

The phase prediction calculations in the CALPHAD method were performed for both equilibrium and non-equilibrium conditions. The simulation results are compared with the experimental data available in the open literature for the respective as-cast, laser clad and thermal sprayed HEAs. As-clad data were used because laser cladding is one of the leading methods to produce HEA coatings. Furthermore, a comparison was also made with phases obtained from HEA coatings developed using the high-velocity oxygen fuel (HVOF) process, as an experimental validation within the scope of the current study. The selection of the HVOF process was based on its lower in-flight oxidation in comparison with other thermal spray methods, such as the atmospheric plasma spray (APS) (Ref 8). Due to the limitations of both empirical models and the CALPHAD method in predicting oxidation, HVOF experimental results can be more conveniently compared with phase predictions if the formation of oxides in the coatings is minimized.

The scope of this study is to discuss the utilization of empirical models and the CALPHAD method for phase prediction in high-entropy alloys under conditions that involve rapid cooling, including casting, laser cladding and thermal spraying. The focus of the research is to evaluate the accuracy of these methods for designing HEAs by comparing the prediction results with the experimental data

available in the open literature and the HVOF coatings produced in this work.

Materials and Methods

Empirical Models

Eight empirical models regarding phase prediction in HEAs were assessed. The four parameter-based models proposed by Zhang et al. (Ref 14), Yang et al. (Ref 16), Guo et al. (Ref 15), and Ye et al. (Ref 22) are the most cited on the Scopus database (see M1 to M4 in Table 1). Two parameter-based models, proposed by Andreoli et al. (Ref 26) and Jiang et al. (Ref 27), were chosen for their capability to predict either the body-centered cubic (BCC) or face-centered cubic (FCC) phases (see M5 and M6 in Table 1). In addition, two free energy-based models, proposed by Troparevsky et al. (Ref 23) and Senkov et al. (Ref 24), were selected based on their higher accuracy in phase prediction for HEAs (see M7 and M8 in Table 1). It is stressed that the ordered BCC phase (B2) is considered to be an intermetallic for all models, except for the one proposed by Guo et al. (Ref 15) which considers the B2 phase as a solid solution.

The solid solution criteria for each of the models assessed in the current study are summarized in Table 1.

Table 2 High-velocity oxygen fuel (HVOF) spray parameters for the development of CoCrFeNi, CoCrFeNiMo$_{0.2}$, CoCrFeNiMo$_{0.5}$, AlCrFeMnNi and AlCoCrFeNi HEA coatings (Ref 44)

HVOF system	GTV HVOF K2, GTV Verschleißschutz GmbH, Germany
Fuel	Kerosene
Fuel flow rate	28 l/min
Oxygen flow rate	950 l/min
Stand-off distance	380 mm
Powder feed rate	50 g/min
Carrier gas	Argon
Carrier gas flow rate	7 l/min

Supplementary Data A presents the respective equations for each model.

ΔH_{mix} and ΔS_{mix} are the enthalpy of mixing and the entropy of mixing for a random solid solution, respectively. δ is the atomic size difference. T_m is the alloy melting temperature. ΔH_{el} is the elastic-strain energy. VEC is the valence electron concentration. T_{ann} is the annealing temperature according to the experimental setting. ΔH_f is the lowest possible formation enthalpy among all the binary element pairs in the alloy. k_1 and k_1^{cr} are defined in Supplementary Data A.

Thermo-Calc Predictions (CALPHAD)

Thermo-Calc v. 2022b (Thermo-Calc Software AB, Stockholm, Sweden), with the TCHEA5.1 equilibrium database and MOBHEA2 mobility database, evaluated the volume fraction of phases as a function of temperature and composition (Ref 43). Equilibrium phase diagrams were plotted to access phase stability for the five HEAs. In addition, phase formation was estimated under non-equilibrium conditions employing Scheil solidification models. The Scheil model assumes that no diffusion occurs in the solid state, while it is infinitely fast in the liquid state. The expected phases for both equilibrium and non-equilibrium simulations were compared to the phases found experimentally in the HVOF coatings as well as with the as-cast, as laser cladded and as thermal sprayed data from the literature.

HVOF Spraying Procedure

Commercially available CoCrFeNi, CoCrFeNiMo$_{0.2}$, CoCrFeNiMo$_{0.5}$, AlCrFeMnNi and AlCoCrFeNi powders (Jiangsu Vilory, China) produced using gas atomization (GA) were employed as the feedstock for the HEA coatings. The feedstock was 15 to 53 μm in size, and the stainless steel substrate (SS316L) was 3 mm thick. The substrate was grit blasted with alumina before spraying. The HEA powders were sprayed with a HVOF thermal spray system (GTV HVOF K2, GTV Verschleißschutz GmbH, Germany) following the spray settings proposed by

Meghwal et al. (Ref 44) shown in Table 2. The coating thicknesses range between 200 and 300 μm.

X-ray Diffraction (XRD)

The D8 Discover Powder x-ray diffraction (XRD) instrument from Bruker performed the phase investigation. The powders and HVOF samples were scanned under Cu Kα radiation over a 2θ scan range of 25°-85° at 40 mA and 40 kV with a 0.05° 2θ step size. XRD patterns were further evaluated in DIFFRAC.SUITE TOPAS 4.2 (Bruker Corp., Billerica, MA, USA) to determine the lattice parameters.

Results and Discussion

The phase predictions for the five HEAs, extrapolated from eight models selected for the empirical approach, are shown in Table 3. The addition of Mo in the CoCrFeNi HEA does not have a considerable impact on the phase predictions, except for the M1, M6 and M7 models. On the other hand, the expected phases are severely influenced by the addition of Al in the CoCrFeNi HEA. For the AlCoCrFeNi HEA, six empirical methods indicate the formation of an intermetallic phase. The substitution of Co for Mn, as shown in the AlCrFeMnNi and AlCoCrFeNi HEAs, has not had any influence on the empirical method predictions. Please refer to Supplementary Data B for the parameter values for each model.

The phases observed in the open literature for the five HEAs in the as-cast condition, and for as-clad, APS and HVOF coatings, are shown in Table 4. In addition, Table 4 also includes the phases observed from the gas atomized powders and HVOF coatings developed in the current study.

It is not uncommon that identical alloy chemistries, prepared by the same manufacturing route but with different process parameters, can result in different phases. For example, four different microstructures are observed in Table 4 for the APS AlCoCrFeNi coatings. For thermal spray, the feedstock production method and spray parameters such as gas flow rate, power input, powder feed rate

Table 3 Phase predictions of the five HEAs for the eight empirical models. The solid solutions in M5 and M6 are FCC-based phase structures

Alloy	M1	M2	M3	M4	M5	M6	M7	M8	Total IM	Total SS
CoCrFeNi	IM	SS	SS	SS	SS	SS	SS	SS	1	7
CoCrFeNiMo$_{0.2}$	SS	SS	SS	SS	SS	SS	IM	SS	1	7
CoCrFeNiMo$_{0.5}$	SS	SS	SS	SS	SS	IM	IM	SS	2	6
AlCrFeMnNi	IM	SS	SS	IM	IM	IM	IM	IM	6	2
AlCoCrFeNi	IM	SS	SS	IM	IM	IM	IM	IM	6	2
Total IM	3	0	0	2	2	3	4	2		
Total SS	2	5	5	3	3	2	1	3		

SS: solid solution, *IM*: intermetallic phase(s).

Table 4 Phases observed within the studied high-entropy alloys produced using melting and casting, laser cladding and thermal spray routes (*LC*: laser cladding, *HVOF*: high-velocity oxygen fuel spray, *APS*: atmospheric plasma spray and *IM*: intermetallic phase(s))

Alloy	Processing route	Phase(s)
CoCrFeNi	GA powder	FCC (current study)
	HVOF	FCC (current study)
	LC	FCC (Ref 45)
	Casting	FCC (Ref 46-48)
CoCrFeNiMo$_{0.2}$	GA powder	FCC (current study)
	HVOF	FCC (current study)
		FCC + oxides (Ref 49)
	APS	FCC + oxides (Ref 49)
	LC	FCC (Ref 50)
		FCC + IM (σ + μ) (Ref 51)
	Casting	FCC (Ref 52-54)
CoCrFeNiMo$_{0.5}$	GA powder	FCC + IM (σ) (current study)
	HVOF	FCC + IM (σ) + oxides (current study)
	Casting	FCC + IM (σ) (Ref 47)
		FCC + IM (σ + μ) (Ref 55)
AlCrFeMnNi	GA powder	BCC + B2 (current study)
	HVOF	BCC + B2 (current study)
	LC	BCC (Ref 56)
	Casting	BCC + B2 (Ref 57-59)
		BCC + B2 + FCC (Ref 60)
AlCoCrFeNi	GA powder	BCC + B2 (current study)
	HVOF	BCC + B2 (current study)
		BCC + B2 (Ref 44)
		BCC + FCC + B2 (Ref 61)
	APS	BCC + FCC + oxides (Ref 62, 63)
		BCC (Ref 64)
		2 BCC + FCC + oxides (Ref 65)
		BCC + FCC + B2 + oxides (Ref 66)
	LC	BCC + FCC (Ref 67, 68)
		BCC + B2 (Ref 69, 70)
	Casting	BCC + B2 (Ref 71)
		B2 (Ref 72)
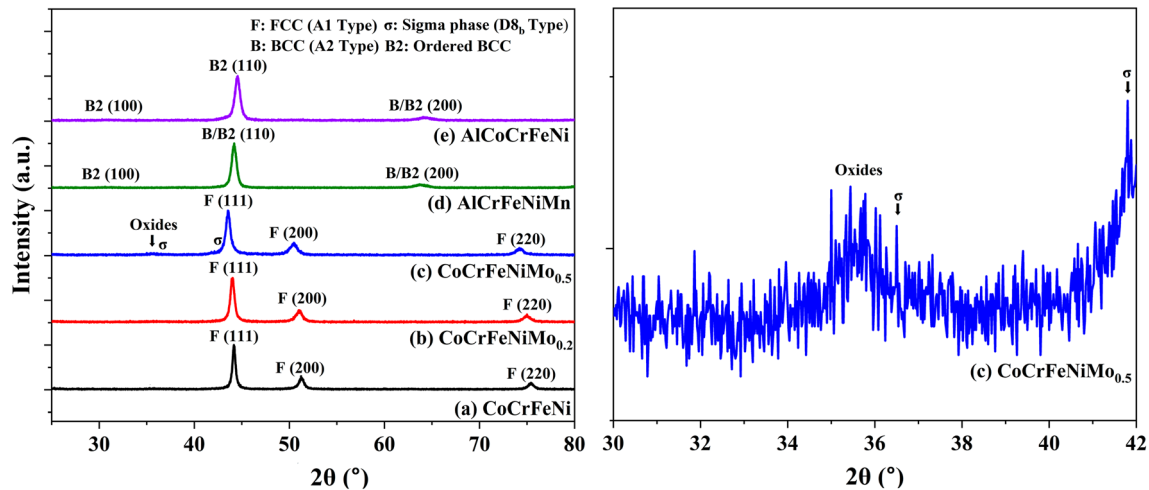
Fig. 1 XRD diffractograms of HVOF (a) CoCrFeNi, (b) CoCrFeNiMo$_{0.2}$, (c) CoCrFeNiMo$_{0.5}$, (d) AlCrFeMnNi and (e) AlCoCrFeNi HEA coatings. An extended view of CoCrFeNiMo$_{0.5}$ is provided for better visualization of the presence of intermetallic phase and oxidation peaks

Table 5 Atomic radius (Ref [4]) for the elements and the mixing enthalpy (Ref [80]) for the possible binaries of the five HEA compositions

Element	Atomic radius, pm	ΔH_{mix}, kJ/mol						
		Fe	Ni	Cr	Co	Mn	Mo	Al
Fe	124.12	…						
Ni	124.59	− 1.6	…					
Cr	124.91	− 1.5	− 6.7	…				
Co	125.10	− 0.6	− 0.2	− 4.5	…			
Mn	135.00	0.2	− 8.2	2.1	− 5.2	…		
Mo	136.26	− 2.0	− 7.3	0.4	− 4.9	4.9	…	
Al	143.17	− 11.1	− 22.3	− 9.9	− 18.8	− 19.1	− 5.1	…

and stand-off distance are critical in determining the coating microstructure (Ref [8]). These TS parameters offer different solidification rates throughout the coating process and, thereby, different phases evolve. Similarly, for vacuum arc melting and casting, the thermal history of the sample is influenced by the arc current, the crucible cooling system and the sample size (Ref [73]). For laser cladding, parameters such as the laser power, the powder feeding rate and the cladding speed influence the phase structure (Ref [74]). The typical cooling rates in processes such as casting, laser cladding and thermal spray are 10 K/s (Ref [75]), 10^3-10^5 K/s (Ref [76]), 10-10^7 K/s (Ref [77]), respectively, depending on the parameters discussed above.

The APS and HVOF processes tend to form oxides due to in-flight oxidation of the feedstock particles (Ref [8]). Oxidation was not considered in our calculations for both empirical and computational approaches. Therefore, the oxides were not considered when comparing the phase predictions with the literature and experimental data.

CoCrFeNi

All empirical methods, except for M1, indicate solid solution formation for CoCrFeNi HEA, as shown in Table [3]. The as-cast and as-clad data from the literature confirm that the CoCrFeNi is primarily a single-phase solid solution based on a FCC phase structure. The XRD diffractogram for HVOF CoCrFeNi coating, shown in Fig. 1(a), demonstrates that the coating spectrum presents peaks related to a major FCC phase. The lattice parameter of the FCC phase is 3.56 Å, which is similar to other CoCrFeNi HEA reports (Ref [46], [47]). Furthermore, (i) the lattice distortion effect, which causes the lattice parameter to fluctuate around an average value, and (ii) the high cooling rates of the HVOF process, leading to strain-induced within splats, are responsible for the peak broadening observed in the diffractogram (Ref [78]). Peak broadening was observed in all HVOF coatings produced in the current study.

The M1 method failed to predict a solid solution for CoCrFeNi because the mixing entropy is 1.39R (11.55 J/K.mol), which lies outside the solid solution criteria of
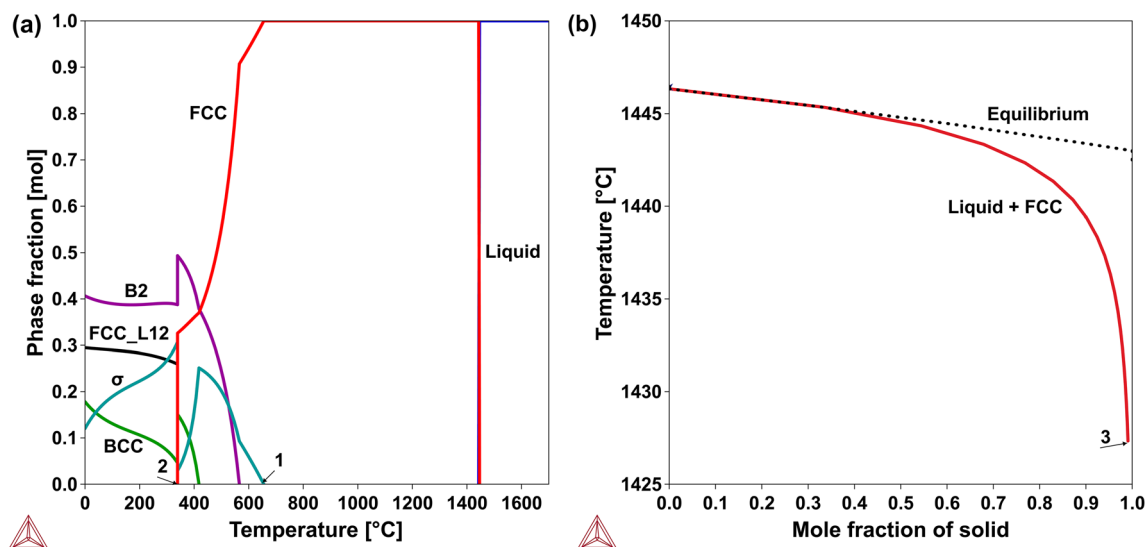
Fig. 2 Phase diagrams as a function of temperature for the CoCrFeNi HEA (a) in equilibrium conditions and (b) Scheil simulation

$12 \leq \Delta S_{mix} \leq 17.5$ J/K.mol. Hence, the M1 model will not be effective in alloys that do not satisfy the configurational entropy definition for HEAs, such as the CoCrFeNi composition.

The similarity between Co, Cr, Fe and Ni elements explains the empirical model's success in predicting the CoCrFeNi phase formation. All the elements are from the fourth period in the periodic table, with their atomic radius ranging from 124.12 pm for iron to 125.10 pm for cobalt, and there is no substantial negative or positive atom pair mixing enthalpy between elements, as can be seen in Table 5. Therefore, the atomic size difference (δ) for this alloy is 0.3% and its ΔH_{mix} is near zero (− 3.78 kJ/mol). According to extensions of Hume-Rothery rules (Ref [79]), near-zero enthalpy of mixing and small atomic size differences are crucial for solid solution formation, which has been observed in most of the models mentioned in Table 3.

An equilibrium phase diagram for the CoCrFeNi alloy is shown in Fig. 2(a). Under equilibrium conditions, the FCC phase dominates after solidification across a wide temperature range. However, at 655 °C (point 1), the sigma phase (σ, the aqua blue line) starts to precipitate. The σ phase is a topologically close-packed (TCP) phase and it is an ubiquitous intermetallic phase in HEAs, especially in the 3d transition metal HEA family (Ref 4, 81). Additional cooling allows the formation of the B2 (purple line), ordered FCC (FCC_L12, black line) and the BCC (green line) phases. Since the FCC phase is unstable below 339 °C (point 2), then σ, B2, ordered FCC, and BCC phases are the only stable phases at room temperature.

The phase prediction resulting from the CALPHAD method using the Scheil simulation is shown in Fig. 2(b). The result illustrates that rapid cooling inhibited the formation of σ, B2, ordered FCC and BCC phases, matching

the results from the literature and HVOF coating produced in the current study, Table 4. The high freezing temperature indicated by the Scheil simulation, 1427 °C (point 3), i.e., where solidification ends, signifies that no other phases form. The freezing/solidification range of the alloy is above the precipitation temperatures of σ, B2, ordered FCC and BCC phases. As seen in the equilibrium diagram, Fig. 2(a), the σ phase starts forming at 655 °C (point 1), a much lower temperature compared to the freezing temperature.

CoCrFeNiMo$_{0.2}$

The CoCrFeNiMo$_{0.2}$ HEA is composed of single-phase FCC in the as-cast condition as shown in Table 4, suggesting that a small amount of Mo in CoCrFeNi HEA does not imply additional phase formation or precipitation. On the other hand, FCC + oxides are observed for both APS and HVOF, and FCC and FCC + σ + μ are observed in LC. No σ or μ phases were observed in the experimental HVOF CoCrFeNiMo$_{0.2}$, as shown in Fig. 1(b). Like the σ phase, the mu (μ) phase is topologically close-packed (TCP) (Ref 79). The μ phase presence in HEAs is not as frequent as the σ phase, but its formation is reported in several alloys, such as CoFeMnMoNi and CoCrFeNiW (Ref 79). The lattice parameter of the FCC phase has slightly increased to 3.58 Å in comparison with 3.56 Å for CoCrFeNi HEA. A similar lattice parameter was observed for another CoCrFeNiMo$_{0.2}$ HEA (Ref 53). More importantly, no peaks related to the presence of oxides were observed in the XRD diffractogram for the CoCrFeNiMo$_{0.2}$ HVOF coating.

Molybdenum exhibits an atomic radius of 136.26 pm, which is greater than the other elements in this alloy (Table 5). However, since the mole percentage of Mo is
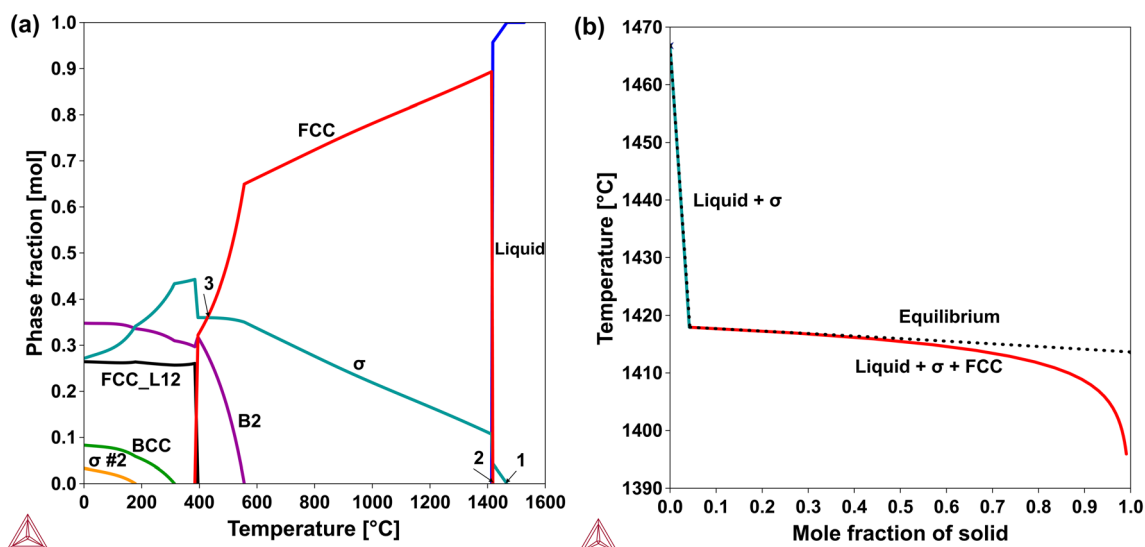
Fig. 3 Phase diagrams as a function of temperature for the CoCrFeNiMo$_{0.2}$ HEA (a) in equilibrium conditions and (b) Scheil simulation

just 4.7% in the CoCrFeNiMo$_{0.2}$ HEA, the resulting δ value is still low, 1.99%. Molybdenum also shows low enthalpy of mixing with the other elements in the alloy, which results in an ΔH$_{mix}$ of −4.09 kJ/mol. These values indicate that the empirical methods, except for M7, predict solid solution formation, which matches the results for the as-cast samples, thermal spray coatings and laser cladding.

M7 is the only empirical parameter that suggests the formation of intermetallic phases in CoCrFeNiMo$_{0.2}$ HEA. The solid solution formation for this model is the inequality -T$_{ann}$ΔS$_{mix}$ < ΔH$_f$ < 37 meV/atom, which is not satisfied because the most stable binary, Fe-Mo, has a formation enthalpy (ΔH$_f$) of −484 meV/atom, while -T$_{ann}$ΔS$_{mix}$ is equal to −137 meV/atom. However, the M7 model can be customized with different annealing temperatures. The annealing temperature selected for the calculations is T$_{ann}$ = 0.55T$_m$, as suggested by the authors (Ref 23). It should be noted, however, that any temperature from T$_{ann}$ = 0.55T$_m$ to T$_{ann}$ = T$_m$ would not change the simulation results for any of the alloys. The equilibrium phase diagram for the CoCrFeNiMo$_{0.2}$ as a function of the temperature is shown in Fig. 3(a). As observed, although the FCC is the primary phase for most temperatures, there is no single-phase region after solidification, suggesting good predictions for the M7 model.

According to the equilibrium phase diagram for the CoCrFeNiMo$_{0.2}$ HEA, the σ phase starts forming at 1486 °C (point 1) as the primary phase. The FCC phase evolved at 1417 °C (point 2), taking over as the primary phase until 426 °C (point 3). At room temperature, B2, σ, ordered FCC (FCC_L12), BCC and σ #2 (yellow line) phases are stable in the equilibrium condition, resulting in a complex structure. Within the Thermo-Calc software,

when there are identical phases present, but with different compositions, they are labelled as #2, #3 and so on. Note that the μ phase, observed in one of the LC coatings, is not in the equilibrium phase diagram at any temperature.

The phase diagram estimated using the Scheil simulation for CoCrFeNiMo$_{0.2}$ HEA is presented in Fig. 3(b). Similar to the equilibrium diagram, the σ phase is the first to be formed, indicating a distinct prediction for what was found in the literature for the as-cast condition, APS and HVOF coatings. However, the FCC is the major phase in the simulation, and the mole percentage of the σ phase is lower than 5%. The σ phase was found in one of the LC coatings, in combination with the FCC and μ phases, suggesting that the σ phase may precipitate for some cooling conditions.

CoCrFeNiMo$_{0.5}$

The addition of Mo$_{0.5}$ into the CoCrFeNi alloy leads to the formation of FCC and intermetallic phases in the as-cast condition, as shown in Table 4. No CoCrFeNiMo$_{0.5}$ HEA has been reported in coating form using either thermal spray or cladding route. The XRD pattern of the HVOF CoCrFeNiMo$_{0.5}$ HEA coating developed in the current study is presented in Fig. 1(c). Major FCC peaks are observed, in addition to minor peaks from a second phase identified as a D8$_b$-type σ phase (JCPDS card number 09-0050). The FCC lattice parameter is 3.60 Å, higher than the lattice parameters identified in the CoCrFeNi and CoCrFeNiMo$_{0.2}$ HEAs, as expected by the Mo content increase. The lattice parameter of the FCC phase is the same as reported by Shun et al. (Ref 47). Iron oxides of Fe$_3$O$_4$ and Fe$_2$O$_3$ and spinels of the form AB$_2$O$_4$ (A = Fe,

Co, Ni and B = Fe, Cr) correspond to the minor oxide peaks, as observed by Li et al. (Ref 49) in both APS and HVOF CoCrFeNiMo$_{0.2}$ coatings.

Six empirical methods, M1, M2, M3, M4, M5 and M8, could not precisely predict the formation of intermetallic phases in the CoCrFeNiMo$_{0.5}$ HEA. With 11.2 at.% Mo, the influence of Mo on the δ and ΔH$_{mix}$ is still very low, calculated to be 2.90% and −4.39 kJ/mol, respectively. Considering these parameters, the CoCrFeNiMo$_{0.5}$ HEA should result in a solid solution, but, in contrast, the additional σ phase is found in the literature and the HVOF coating in the current study, Table 4. Tsai et al. (Ref 79) state that stable IM phases arise when there is a large negative mixing enthalpy between two elements, but the opposite outcome is not necessarily true. In fact, σ and μ phases can have near-zero enthalpy of mixing (Ref 79). In addition, phases such as σ and μ can be formed between elements with minor atomic size differences, sometimes causing misguided predictions when δ and ΔH$_{mix}$ are used as parameters to filter the σ and μ phases, as observed for M1, M2, M3 and M4 models. The precipitation of hard and brittle σ and μ intermetallic compounds can negatively influence the alloy's mechanical properties, such as reducing the fracture toughness (Ref 82, 83). Therefore, predicting σ and μ phase formation and controlling their volume fractions becomes crucial.

Tsai et al. (Ref 81) proposed an empirical model to predict the σ phase formation in HEAs consisting of two criteria, (i) the valence electron concentration (VEC) is between 6.88 and 7.84, and (ii) the content of the paired sigma-forming element (PSFE) is higher than 40 at.%. The σ phase will only form if both conditions are satisfied. The VEC calculated for CoCrFeNiMo$_{0.5}$ HEA is 8, outside of

the sigma-forming range, and its PSFE is 66.6%. Thus, the alloy does not satisfy the empirical model criteria proposed by Tsai et al. (Ref 81). However, it has been suggested that Mo-containing alloys can have distinct sigma-forming VEC ranges (Ref 84), but the authors proposed no new criterion range.

The empirical model M6 is the only parameter-based model to predict the intermetallic formation in CoCrFeNiMo$_{0.5}$ HEA. Although the two parameters for solid solution formation in this model, δ and ΔH$_{mix}$, are satisfied, the VEC, which is used to determine the alloy crystal structure, is not fulfilled. As mentioned above, the VEC for CoCrFeNiMo$_{0.5}$ is 8, and FCC is only formed in the case of VEC > 8, according to the model. Furthermore, the elastic-strain energy criterion, ΔH$_{el}$, used in model M5 as the topological parameter, could also not predict σ formation.

As observed for CoCrFeNiMo$_{0.2}$ in Table 3, the M7 model suggests the formation of intermetallic phases because the most stable binary, Fe-Mo, has an ΔH$_f$ of −484 meV/atom, while -T$_{ann}$ΔS$_{mix}$ is equal to −148 meV/atom. On the other hand, M8, which is also a free energy-based model, predicts the formation of a solid solution. The criterion for solid solution formation on M8 is k$_1$ < k$_1^{cr}$, in which k$_1^{cr}$ and k$_1$ represent the Gibbs free energy for the solid solution, and the hypothetical intermetallic phase, respectively. For the CoCrFeNiMo$_{0.5}$ alloy, k$_1^{cr}$ = 2.30, and k$_1$ = 2.20, satisfying the M8 criterion, therefore, indicating solid solution formation in the CoCrFeNiMo$_{0.5}$ HEA.

Within the computational approach, the equilibrium phase diagram for CoCrFeNiMo$_{0.5}$, Fig. 4(a), exhibits similar patterns as for the CoCrFeNiMo$_{0.2}$ HEA. The σ phase is the first to be formed at 1689 °C (point 1), but the
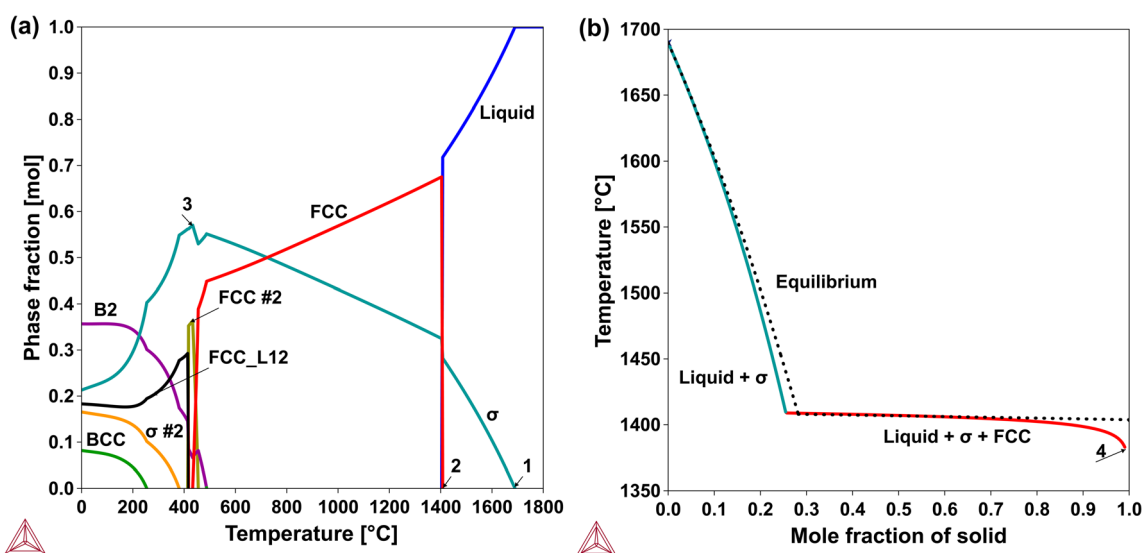
Fig. 4 Phase diagrams as a function of temperature for the CoCrFeNiMo$_{0.5}$ HEA (a) in equilibrium conditions and (b) Scheil simulation
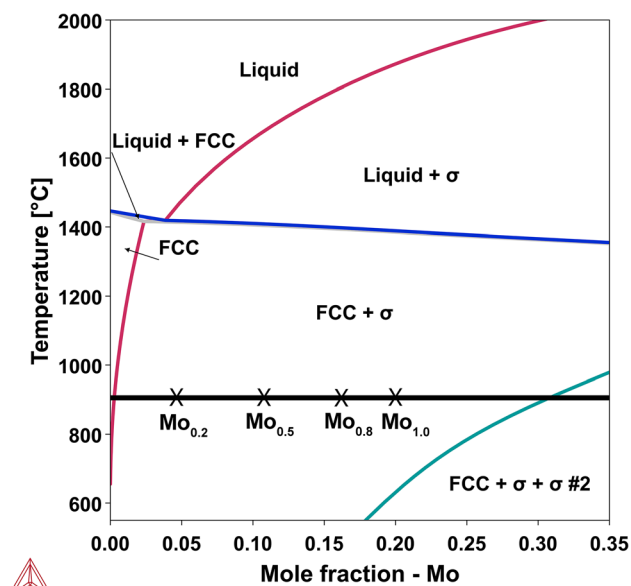
Fig. 5 The equilibrium pseudo-binary phase diagram of the (CoCrFeNi)-Mo alloy system. The CoCrFeNiMo$_x$ ($x = 0.2, 0.5, 0.8,$ 1) at 900 °C are marked in the phase diagram

FCC phase dominates after its formation at 1407 °C (point 2). The increase of Mo from 4.8 at.% in the CoCrFeNiMo$_{0.2}$ to 11.1 at.% in the CoCrFeNiMo$_{0.5}$ makes the σ phase prevalent at a higher temperature, reaching 57% of the molar phase fraction at 433 °C (point 3). At room temperature, B2, σ, ordered FCC (FCC_L12), BCC and σ #2 phases are stable at equilibrium.

The Scheil simulation for CoCrFeNiMo$_{0.5}$ is presented in Fig. 4(b). The σ phase is the first to be formed at a higher temperature as observed in the Scheil simulation of CoCrFeNiMo$_{0.2}$ HEA, Fig. 3(b). The mole fraction of the σ phase is approximately 25%, which solidifies from 1690 to 1409 °C. The only other phase predicted to form is FCC. The formation of all other phases was suspended due to rapid cooling and their lower precipitation temperatures. According to the Scheil simulation, the alloy solidification ends at 1383 °C (point 4). The temperature at which the alloy solidifies completely is much higher than the B2 precipitation temperature, 487 °C, which is the first phase to be formed after the σ and FCC phases, as indicated by the equilibrium diagram. However, Scheil simulations assume no diffusion after complete solidification of the alloy; therefore, phases other than σ and FCC have not been predicted by the simulation.

The μ phase observed in one of the as-cast HEAs (Table 4) is present in neither the equilibrium phase diagram nor the Scheil simulation, which suggests mispredictions related to μ phase precipitation might occur when using the TCHEA5.1 database. In fact, although the μ phase is one of the input phases in the TCHEA5.1 database, it does not form at higher temperatures of the pseudo-

binary phase diagram of the (CoCrFeNi)-Mo alloy system as shown in Fig. 5. Niu et al. (Ref 85) studied the microstructural evolution of CoCrFeNiMo$_x$ HEA ($x = 0.2,$ 0.5, 0.8, 1) annealed at 900 °C. In the CoCrFeNiMo$_{0.2}$ HEA, the σ phase precipitates in the FCC matrix. In addition, the μ phase is formed in CoCrFeNiMo$_{0.5}$, with another σ phase precipitating in both CoCrFeNiMo$_{0.8}$ and CoCrFeNiMo. According to the Thermo-Calc equilibrium pseudo-binary phase diagram, all of the CoCrFeNiMo$_x$ ($x = 0.2,$ 0.5, 0.8, 1) alloys annealed at 900 °C would present an FCC + σ phase, pointing out to the necessity of a critical assessment for the Co-Cr-Fe-Mo-Ni alloy system, especially when it comes to the evolution of μ phase and the phase stability of σ #2 phase.

AlCrFeMnNi

As shown in Table 4, the phases observed for AlCrFeMnNi HEA in the literature are BCC + B2 and BCC + B2 + FCC for the as-cast condition and BCC + B2 and BCC for the HVOF and LC samples, respectively. The XRD pattern for the HVOF AlCrFeMnNi HEA coating fabricated in the current study is shown in Fig. 1(d). The alloy displays BCC/B2 peaks with a lattice parameter of 2.90 Å, which is similar to the BCC lattice parameter (2.89 Å) reported by Zhang et al. (Ref 56).

Aluminum is known as a BCC stabilizer, and its presence in the alloy promotes BCC/B2 formation (Ref 86). Out of 72 HEAs published in the literature with the B2 phase structure, 71 contained Al in their compositions. It is suggested that the BCC ordering occurs due to the strong atomic interaction between Al and other elements (Ref 12), as can be verified with the mixing enthalpy between Al and other elements in Table 5. In fact, on the binary diagrams of the elements in the AlCrFeMnNi alloy, the B2 phase is found in the Al-Fe, Al-Ni and Al-Mn diagrams, attributing the strong feasibility of B2 phase structure formation in AlCrFeMnNi HEA composition.

The negative mixing enthalpy, especially for the Al-Ni and Al-Mn pairs, and the larger atomic radius of Al compared to Cr, Fe, Ni and Mn, have an important influence on ΔH_{mix} and δ, respectively. The ΔH_{mix} of AlCrFeMnNi is −12.50 kJ/mol, and its δ is 5.80%. Therefore, six empirical models, Table 3, indicate the formation of intermetallic phases; i.e., B2 is formed. For some of the parameter-based models that use both δ and ΔH_{mix}, such as M1 and M4, the δ is the critical criterion that indicates intermetallic formation since the ΔH_{mix} value is inside the solid solution ranges. On the other hand, none of the three criteria, δ, ΔH_{mix} and the valence electron concentration (VEC), were satisfied in the M6 method. As mentioned above, the M3 model considers the B2 phase as a solid solution, which explains its less strict criteria for solid solution formation.
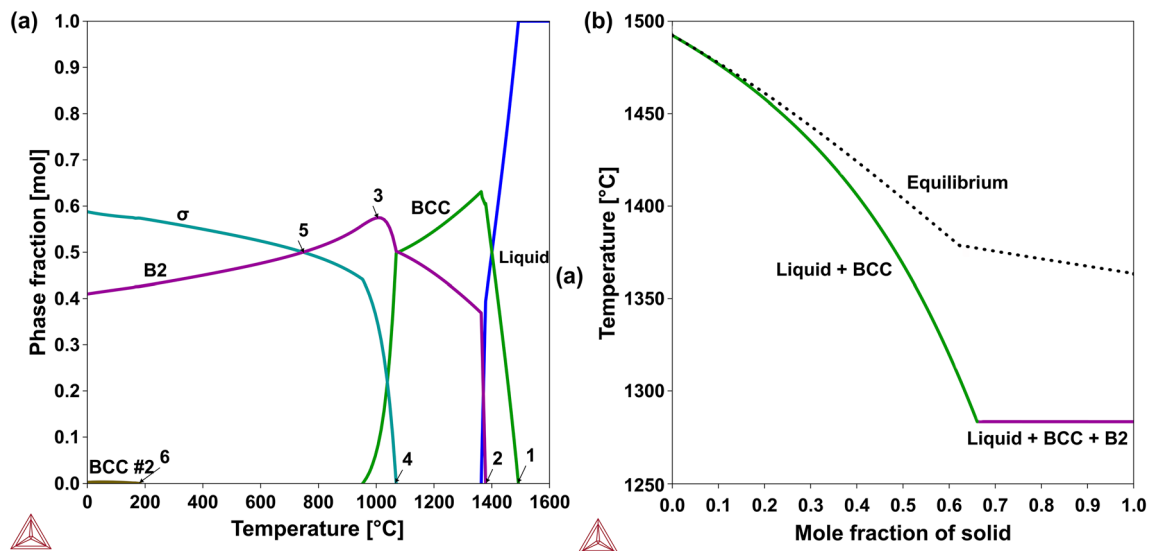
Fig. 6 Phase diagrams as a function of temperature for the AlCrFeMnNi HEA (a) in equilibrium conditions and (b) Scheil simulation

M2 was the only model that predicted a solid solution phase for the AlCrFeMnNi alloy due to a broader δ superior range, 6.6%, than the other models that use δ to filter the intermetallic formation.

For the free energy-based models, M7 and M8, their proposed hypothetical intermetallic compounds are strongly affected by the Al addition. For M7, the most stable binary, Al-Ni, has an ΔH_f of −677 meV/atom, while $-T_{ann}\Delta S_{mix}$ equals −124 meV/atom. Thus, the inequality criterion is not satisfied. For M8, the high mixing enthalpy between the elements severely drops k_1^{cr}, and the high formation enthalpy (ΔH_{IM}) increases k_1. Therefore, $k_1 > k_1^{cr}$, and so intermetallic formation is expected for AlCrFeMnNi HEA.

An equilibrium phase diagram for the AlCrFeMnNi alloy is displayed in Fig. 6(a). The first phase to be formed on cooling from the liquid is the BCC phase at 1492 °C (point 1). Additional cooling leads to the formation of the B2 phase at 1379 °C (point 2), reaching a maximum of 56% of the phase fraction of the alloy at 1007 °C (point 3). The growth of the B2 phase fraction occurs as the amount of the BCC phase decreases. The σ phase starts precipitating at 1069 °C (point 4) and becomes the major phase at 806 °C (point 5). A new BCC phase (brown line) is formed at 182 °C (point 6), with a maximum phase fraction of 0.03% at 66 °C. Note that the FCC phase is found in one of the as-cast HEAs, but it is not observed in the equilibrium phase diagram at any temperature.
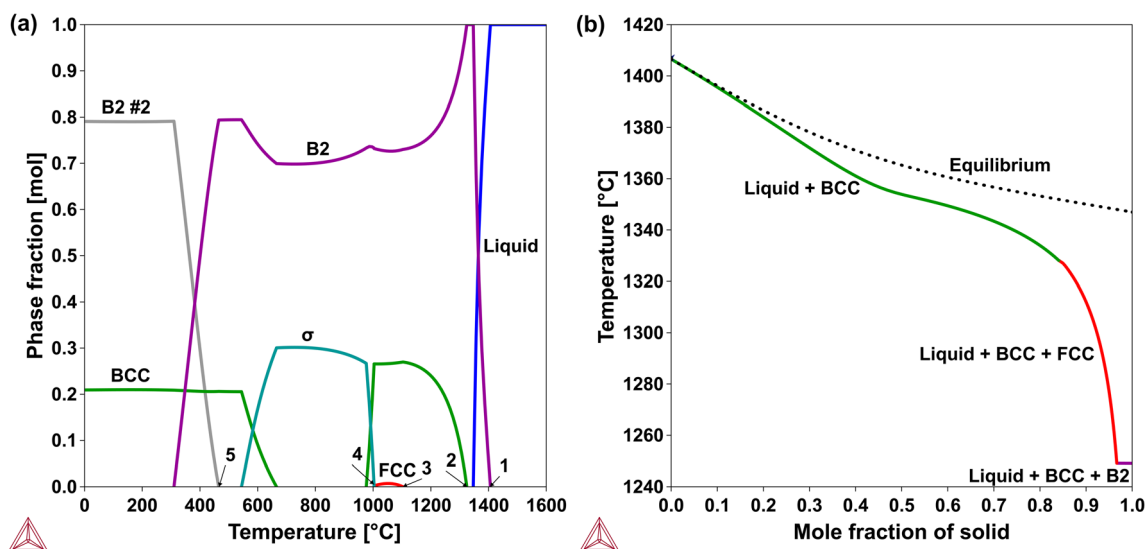
The Scheil simulation for the AlCrFeMnNi alloy, presented in Fig. 6(b), indicates that the σ phase formation has been suppressed during solidification with rapid cooling rates. The non-equilibrium diagram complements the phase structure observed in the HVOF coating manufactured in the current study. The LC coating, which shows a single-phase BCC, could have formed at a much higher cooling rate than thermal spraying, thereby further suppressing the BCC ordering (B2 phase).

AlCoCrFeNi

The AlCoCrFeNi HEA system has been documented in the open literature. The phases observed for AlCoCrFeNi HEA are BCC + B2, and B2 in the as-cast condition, BCC + FCC, and BCC + B2 for the LC coatings, BCC + FCC + oxides, single-phase BCC, 2BCC + FCC + oxides and BCC + FCC + B2 + oxides for the APS coatings, BCC + B2 and BCC + FCC + B2 for the HVOF coatings. The XRD pattern of the HVOF AlCoCrFeNi HEA coating is presented in Fig. 1(e), displaying peaks corresponding to BCC/B2 with a lattice parameter of 2.89 Å. The lattice parameters of the BCC/B2 phases are the same as the AlCoCrFeNi HVOF coating reported by Meghwal et al. (Ref 44).

The substitution of Mn with Co in AlCrFeMnNi to form AlCoCrFeNi has a low influence on the total mixing enthalpy since the Mn and Co binary enthalpies among the other alloying elements are similar, as shown in Table 5. Therefore, the ΔH_{mix} for the AlCoCrFeNi HEA is −12.30 kJ/mol, which is comparable to ΔH_{mix} for AlCrFeMnNi (− 12.50 kJ/mol). In addition, Co has a similar atomic size to Cr, Fe and Ni, when compared to Mn. However, Mn has a more comparable atomic size to Al. Thus, only a small decrease in δ for AlCoCrFeNi (5.77%) is observed as compared to AlCrFeMnNi (5.82%), favoring similar phase formation predictions for both HEAs.

Fig. 7 Phase diagrams as a function of temperature for the AlCoCrFeNi HEA (a) in equilibrium conditions and (b) Scheil simulation

None of the empirical model predictions (Table 3) for the AlCrFeMnNi HEA changed for the AlCoCrFeNi HEA composition. The similar ΔH_{mix} and δ values for both alloys explain the same phase predictions for the models that use these two parameters to filter intermetallic phases. The VEC and ΔH_{el} are also not heavily affected by substituting Mn for Co, which justifies similar phase predictions for M5 and M6 models. For M7, the most stable binary, the Al-Ni system, is the same as for the AlCrFeMnNi HEA and the $-T_{ann}\Delta S_{mix}$ value is not enough to satisfy the model inequality. For the M8 model, the mixing enthalpy for the intermetallic is higher than for the AlCrFeMnNi alloy, which increases k_1, and so intermetallic formation is expected.

All phases observed in the literature and the HVOF coating were found within temperature ranges in the CALPHAD equilibrium phase diagram, as shown in Fig. 7(a). The B2 phase is the first to be formed at 1406 °C (point 1) and is the major phase after solidification. With cooling, the B2 phase is followed by the BCC phase at 1324 °C (point 2). Subsequently, the FCC and σ phases are formed at 1103 °C (point 3) and 1003 °C (point 4), respectively. In addition, a new B2 phase, B2 #2 (grey line), is formed at 465 °C (point 5), and its growth takes place at the expense of the initial B2 phase. The BCC and B2 #2 phases are stable at room temperature.

The Scheil simulation for AlCoCrFeNi is presented in Fig. 7(b). All the phases observed in the literature and the HVOF coating were discovered in the non-equilibrium simulation. The final phase structure in Scheil simulation is composed of BCC + FCC + B2 phases, which are the same mentioned phases as reported in the APS AlCoCr-FeNi HEA by Meghwal et al. (Ref 66) and HVOF AlCoCrFeNi HEA by Löbel et al. (Ref 61) (Table 4). Note

that the formation of the intermetallic σ phase was suspended due to rapid cooling.

In a summary, the empirical models and the CALPHAD method exhibited good efficiency in predicting phase formation in HEA coatings. The higher cooling rate in the TS and LC processes, compared to casting, had only a small influence on the phases formed. In designing HEA compositions, Fe, Ni, Co, Cr and Al are the most explored elements (Ref 4). The alloys in the current study are also mainly composed of these elements; therefore, the accuracy of the models may have improved, since the experimental data available in the literature are essential to the development of these models. In fact, the CoCrFeNi, AlCoCrFeNi and CoCrFeNiMo$_{0.5}$ compositions are present in some of the model databases. Furthermore, the CoCr-FeNi and AlCoCrFeNi HEAs were used in the TCHEA database validation. Note that the addition of Mo, which is an element that is not as common in HEA compositions, already led to incorrect predictions in some of the empirical models and the CALPHAD method. Therefore, caution is recommended when using empirical models and the CALPHAD method for phase prediction of alloys that contain less used elements in HEAs.

Conclusions

Five high-entropy alloys were studied: CoCrFeNi, CoCrFeNiMo$_{0.2}$, CoCrFeNiMo$_{0.5}$, AlCrFeMnNi and AlCoCrFeNi. Phase predictions were performed by empirical models and the CALPHAD method under equilibrium and non-equilibrium conditions. The phase predictions were correlated with experimental data for as-cast, laser clad and thermal sprayed HEAs. The empirical and

computational approaches were validated by the experimental results in the form of phases observed in HVOF coatings. The main conclusions follow:

(a) Despite the cooling rate differences between casting, laser cladding and thermal spraying, similar phase formation is observed for each of the compositions.

(b) The empirical models successfully predict solid solution formation for the CoCrFeNi HEAs due to the similarity between the elements. Furthermore, the phase diagram from the Scheil simulation confirms that a single-phase FCC is formed, matching the experimental observations.

(c) The small atomic size difference and a near-zero mixing enthalpy for the σ and μ phases may cause phase misprediction by the parameter-based models, as observed for the $CoCrFeNiMo_{0.2}$ and $CoCrFeNiMo_{0.5}$ HEAs. In addition, incorrect predictions related to the μ phase precipitation were observed for equilibrium and non-equilibrium CALPHAD phase diagrams. On the other hand, the FCC and σ phases for the $CoCrFeNiMo_{0.5}$ HEA are correctly predicted by the Scheil simulation and were experimentally validated.

(d) The significant influence of Al on the empirical model parameters due to its larger atomic radius and negative enthalpy of mixing assists in accurate intermetallic predictability for AlCrFeMnNi and AlCoCrFeNi. In addition, the phase diagrams from the Scheil simulations for both alloys are validated by the experimental results.

(e) The CALPHAD equilibrium diagrams correctly predicted all the major phases in the alloys at specified temperatures. The exceptions are the minor phases of (i) the μ phase for the $CoCrFeNiMo_{0.2}$ and $CoCrFeNiMo_{0.5}$ alloys, and (ii) the FCC phase for the AlCrFeMnNi. Additionally, Scheil simulations successfully predicted all the phases observed in the HEA coatings, except for the μ phase.

(f) For all the alloys, the rapid cooling in casting, HVOF and laser cladding processing routes inhibited the formation of predicted phases in the equilibrium diagrams. Therefore, the Scheil simulations, which assume no diffusion after complete solidification, are more accurate when comparing the results from the literature and HVOF coating produced in the current study.

The empirical models and the CALPHAD method exhibited good efficiency in predicting the phase formation of the HEA coatings examined in this study. Further research should explore their accuracy with coatings composed of less commonly used elements in the HEA field, and from other HEA families, such as refractory HEAs. Additionally, future studies should focus on employing the Scheil simulations to quantitatively compare simulated phase formation with experimental results from non-equilibrium processing routes. Conducting these studies would enhance the understanding of the capabilities and limitations of the empirical models and the CALPHAD method, thus facilitating HEA design.

References

1. E.P. George, D. Raabe, and R.O. Ritchie, High-Entropy Alloys, *Nat. Rev. Mater.*, 2019, **4**(8), p 515-534. https://doi.org/10.1038/s41578-019-0121-4

2. S. Gorsse, D.B. Miracle, and O.N. Senkov, Mapping the World of Complex Concentrated Alloys, *Acta Mater.*, 2017, **135**, p 177-187.

3. M.H. Tsai and J.W. Yeh, High-Entropy Alloys: A Critical Review, *Mater. Res. Lett.*, 2014, **2**(3), p 107-123. https://doi.org/10.1080/21663831.2014.912690

4. D.B. Miracle and O.N. Senkov, A Critical Review of High Entropy Alloys and Related Concepts, *Acta Mater.*, 2017, **122**, p 448-511. https://doi.org/10.1016/j.actamat.2016.08.081

5. P. Sharma, V.K. Dwivedi, and S.P. Dwivedi, Development of High Entropy Alloys: A Review, *Mater. Today Proc.*, 2021, **43**, p 502-509.

6. W. Zhang, P.K. Liaw, and Y. Zhang, Science and Technology in High-Entropy Alloys, *Sci. China Mater.*, 2018, **61**(1), p 2-22. https://doi.org/10.1007/S40843-017-9195-8

7. Y. Zhang, T.T. Zuo, Z. Tang, M.C. Gao, K.A. Dahmen, P.K. Liaw, and Z.P. Lu, Microstructures and Properties of High-Entropy Alloys, *Prog. Mater. Sci.*, 2014, **61**, p 1-93.

8. A. Meghwal, A. Anupam, B.S. Murty, C.C. Berndt, R.S. Kottada, and A.S.M. Ang, Thermal Spray High-Entropy Alloy Coatings: A Review, *J. Therm. Spray Technol.*, 2020, **29**(5), p 857-893. https://doi.org/10.1007/s11666-020-01047-0

9. J.-W. Yeh, S.-J. Lin, T.-S. Chin, J.-Y. Gan, S.-K. Chen, T.-T. Shun, C.-H. Tsau, and S.-Y. Chou, Formation of Simple Crystal Structures in Cu-Co-Ni-Cr-Al-Fe-Ti-V Alloys with Multiprincipal Metallic Elements, *Metall. Mater. Trans. A*, 2004, **35**(8), p 2533-2536. https://doi.org/10.1007/s11661-006-0234-4

10. J.-W. Yeh, S.-K. Chen, S.-J. Lin, J.-Y. Gan, T.-S. Chin, T.-T. Shun, C.-H. Tsau, and S.-Y. Chang, Nanostructured High-Entropy Alloys with Multiple Principal Elements: Novel Alloy Design Concepts and Outcomes, *Adv. Eng. Mater.*, 2004, **6**(5), p 299-303. https://doi.org/10.1002/adem.200300567

11. S. Gorsse, M.H. Nguyen, O.N. Senkov, and D.B. Miracle, Database on the Mechanical Properties of High Entropy Alloys and Complex Concentrated Alloys, *Data Brief*, 2018, **21**, p 2664-2678.

12. O.N. Senkov, D.B. Miracle, K.J. Chaput, and J.P. Couzinie, Development and Exploration of Refractory High Entropy Alloys—A Review, *J. Mater. Res.*, 2018, **33**(19), p 3092-3128.

13. W. Steurer, Single-Phase High-Entropy Alloys—A Critical Update, *Mater. Charact.*, 2020, **162**, p 110179.

14. Y. Zhang, Y.J. Zhou, J.P. Lin, G.L. Chen, and P.K. Liaw, Solid-Solution Phase Formation Rules for Multi-Component Alloys, *Adv. Eng. Mater.*, 2008, **10**(6), p 534-538.

15. S. Guo and C.T. Liu, Phase Stability in High Entropy Alloys: Formation of Solid-Solution Phase or Amorphous Phase, *Prog. Nat. Sci. Mater. Int.*, 2011, **21**(6), p 433-446.

16. X. Yang and Y. Zhang, Prediction of High-Entropy Stabilized Solid-Solution in Multi-Component Alloys, *Mater. Chem. Phys.*, 2012, **132**(2-3), p 233-238.

17. S. Guo, Q. Hu, C. Ng, and C.T. Liu, More than Entropy in High-Entropy Alloys: Forming Solid Solutions or Amorphous Phase, *Intermet. (Barking)*, 2013, **41**, p 96-103.

18. M.X. Ren, B.S. Li, and H.Z. Fu, Formation Condition of Solid Solution Type High-Entropy Alloy, *Trans. Nonferrous Metals Soc. China*, 2013, **23**(4), p 991-995.

19. A.K. Singh, N. Kumar, A. Dwivedi, and A. Subramaniam, A Geometrical Parameter for the Formation of Disordered Solid Solutions in Multi-Component Alloys, *Intermet. (Barking)*, 2014, **53**, p 112-119.

20. Y.F. Ye, Q. Wang, J. Lu, C.T. Liu, and Y. Yang, Design of High Entropy Alloys: A Single-Parameter Thermodynamic Rule, *Scr. Mater.*, 2015, **104**, p 53-55.

21. Z. Wang, Y. Huang, Y. Yang, J. Wang, and C.T. Liu, Atomic-Size Effect and Solid Solubility of Multicomponent Alloys, *Scr. Mater.*, 2015, **94**, p 28-31.

22. Y.F. Ye, Q. Wang, J. Lu, C.T. Liu, and Y. Yang, High-Entropy Alloy: Challenges and Prospects, *Mater. Today*, 2016, **19**(6), p 349-362.

23. M.C. Troparevsky, J.R. Morris, P.R.C. Kent, A.R. Lupini, and G.M. Stocks, Criteria for Predicting the Formation of Single-Phase High-Entropy Alloys, *Phys. Rev. X*, 2015, **5**(1), p 11041. https://doi.org/10.1103/PhysRevX.5.011041

24. O.N. Senkov and D.B. Miracle, A New Thermodynamic Parameter to Predict Formation of Solid Solution or Intermetallic Phases in High Entropy Alloys, *J. Alloys Compd.*, 2016, **658**, p 603-607.

25. D.J.M. King, S.C. Middleburgh, A.G. McGregor, and M.B. Cortie, Predicting the Formation and Stability of Single Phase High-Entropy Alloys, *Acta Mater.*, 2016, **104**, p 172-179.

26. A.F. Andreoli, J. Orava, P.K. Liaw, H. Weber, M.F. de Oliveira, K. Nielsch, and I. Kaban, The Elastic-Strain Energy Criterion of Phase Formation for Complex Concentrated Alloys, *Mater. (Oxf)*, 2019, **5**, p 100222. https://doi.org/10.1016/j.mtla.2019.100222

27. L. Jiang, Y.P. Lu, H. Jiang, T.M. Wang, B.N. Wei, Z.Q. Cao, and T.J. Li, Formation Rules of Single Phase Solid Solution in High Entropy Alloys, *Mater. Sci. Technol.*, 2016, **32**(6), p 588-592. https://doi.org/10.1179/1743284715Y.0000000130

28. O.N. Senkov, C. Zhang, A.L. Pilchak, E.J. Payton, C. Woodward, and F. Zhang, CALPHAD-Aided Development of Quaternary Multi-Principal Element Refractory Alloys Based on NbTiZr, *J. Alloys Compd.*, 2019, **783**, p 729-742.

29. C. Zhang and M.C. Gao, CALPHAD Modeling of High-Entropy Alloys, *High-Entropy Alloys: Fundamentals and Applications*, in M. Gao, JW. Yeh, P. Liaw, and Y. Zhang (eds.), Springer, Berlin, 2016, pp. 399-444

30. S. Gorsse and F. Tancret, Current and Emerging Practices of CALPHAD Toward the Development of High Entropy Alloys and Complex Concentrated Alloys, *J. Mater. Res.*, 2018, **33**(19), p 2899-2923. https://doi.org/10.1557/jmr.2018.152

31. Y. Zhang and Y.J. Zhou, Solid Solution Formation Criteria for High Entropy Alloys, *Mater. Sci. Forum*, 2007, **561-565**, p 1337-1339. https://doi.org/10.4028/www.scientific.net/MSF.561-565.1337

32. S. Guo, C. Ng, J. Lu, and C.T. Liu, Effect of Valence Electron Concentration on Stability of Fcc or Bcc Phase in High Entropy Alloys, *J. Appl. Phys.*, 2011, **109**(10), p 103505.

33. J.H. Li and M.H. Tsai, Theories for Predicting Simple Solid Solution High-Entropy Alloys: Classification, Accuracy, and Important Factors Impacting Accuracy, *Scr. Mater.*, 2020, **188**, p 80-87.

34. B.S. Murty, J.W. Yeh, S. Ranganathan, and P.P. Bhattacharjee, Synthesis and Processing, *High-Entropy Alloys*, in B.S. Murty, J.W. Yeh, S. Ranganathan, and P.P. Bhattacharjee (eds.) 2nd ed., Elsevier, 2019, pp. 103-117

35. O.N. Senkov, J.D. Miller, D.B. Miracle, and C. Woodward, Accelerated Exploration of Multi-Principal Element Alloys for Structural Applications, *Calphad*, 2015, **50**, p 32-48.

36. O.N. Senkov, J.D. Miller, D.B. Miracle, and C. Woodward, Accelerated Exploration of Multi-Principal Element Alloys with Solid Solution Phases, *Nat. Commun.*, 2015, **6**(1), p 1-10. https://doi.org/10.1038/ncomms7529

37. J.O. Andersson, T. Helander, L. Höglund, P. Shi, and B. Sundman, Thermo-Calc & DICTRA, Computational Tools for Materials Science, *Calphad*, 2002, **26**(2), p 273-312.

38. S.L. Chen, S. Daniel, F. Zhang, Y.A. Chang, X.Y. Yan, F.Y. Xie, R. Schmid-Fetzer, and W.A. Oates, The PANDAT Software Package and Its Applications, *Calphad*, 2002, **26**(2), p 175-188.

39. E. Scheil, Bemerkungen Zur Schichtkristallbildung, *Int. J. Mater. Res.*, 1942, **34**(3), p 70-72. https://doi.org/10.1515/IJMR-1942-340303

40. S.L. Chen, Y. Yang, S.W. Chen, X.G. Lu, and Y.A. Chang, Solidification Simulation Using Scheil Model in Multicomponent Systems, *J. Phase Equilibria Diffus.*, 2009, **30**(5), p 429-434. https://doi.org/10.1007/S11669-009-9568-0

41. J. Li, Y. Huang, X. Meng, and Y. Xie, A Review on High Entropy Alloys Coatings: Fabrication Processes and Property Assessment, *Adv. Eng. Mater.*, 2019, **21**(8), p 1900343. https://doi.org/10.1002/ADEM.201900343

42. C. Dai, T. Zhao, C. Du, Z. Liu, and D. Zhang, Effect of Molybdenum Content on the Microstructure and Corrosion

Behavior of FeCoCrNiMox High-Entropy Alloys, *J. Mater. Sci. Technol.*, 2020, **46**, p 64-73.

43. "Thermo-Calc Software, TCHEA5.1, MOBHEA2: High Entropy Alloys Database," 2022, https://www.thermocalc.com/products/databases/high-entropy-alloys/. Accessed 16 September 2022

44. A. Meghwal, S. Singh, A. Anupam, H.J. King, C. Schulz, C. Hall, P. Munroe, C.C. Berndt, and A.S.M. Ang, Nano- and Micro-Mechanical Properties and Corrosion Performance of a HVOF Sprayed AlCoCrFeNi High-Entropy Alloy Coating, *J. Alloys Compd.*, 2022, **912**, p 165000.

45. Q. Zhu, Y. Liu, and C. Zhang, Laser Cladding of CoCrFeNi High-Entropy Alloy Coatings: Compositional Homogeneity towards Improved Corrosion Resistance, *Mater. Lett.*, 2022, **318**, p 132133.

46. A. Verma, P. Tarate, A.C. Abhyankar, M.R. Mohape, D.S. Gowtam, V.P. Deshmukh, and T. Shanmugasundaram, High Temperature Wear in CoCrFeNiCux High Entropy Alloys: The Role of Cu, *Scr. Mater.*, 2019, **161**, p 28-31.

47. T.T. Shun, L.Y. Chang, and M.H. Shiu, Microstructure and Mechanical Properties of Multiprincipal Component CoCrFeNi-Mox Alloys, *Mater. Charact.*, 2012, **70**, p 63-67.

48. Y.F. Kao, T.J. Chen, S.K. Chen, and J.W. Yeh, Microstructure and Mechanical Property of As-Cast, -Homogenized, and -Deformed AlxCoCrFeNi (0 ≤ x ≤ 2) High-Entropy Alloys, *J. Alloys Compd.*, 2009, **488**(1), p 57-64.

49. T. Li, Y. Liu, B. Liu, W. Guo, and L. Xu, Microstructure and Wear Behavior of FeCoCrNiMo0.2 High Entropy Coatings Prepared by Air Plasma Spray and the High Velocity Oxy-Fuel Spray Processes, *Coatings*, 2017, **7**(9), p 151. https://doi.org/10.3390/COATINGS7090151

50. H. Wu, S. Zhang, Z.Y. Wang, C.H. Zhang, H.T. Chen, and J. Chen, New Studies on Wear and Corrosion Behavior of Laser Cladding FeNiCoCrMox High Entropy Alloy Coating: The Role of Mo, *Int. J. Refract. Metals Hard Mater.*, 2022, **102**, p 105721.

51. W. Li, W. Guo, H. Zhang, H. Xu, L. Chen, J. Zeng, B. Liu, and Z. Ding, Influence of Mo on the Microstructure and Corrosion Behavior of Laser Cladding FeCoCrNi High-Entropy Alloy Coatings, *Entropy*, 2022, **24**(4), p 539. https://doi.org/10.3390/E24040539

52. W. Wang, J. Wang, Z. Sun, J. Li, L. Li, X. Song, X. Wen, L. Xie, and X. Yang, Effect of Mo and Aging Temperature on Corrosion Behavior of (CoCrFeNi)100-XMox High-Entropy Alloys, *J. Alloys Compd.*, 2020, **812**, p 152139.

53. W.H. Liu, Z.P. Lu, J.Y. He, J.H. Luan, Z.J. Wang, B. Liu, Y. Liu, M.W. Chen, and C.T. Liu, Ductile CoCrFeNiMox High Entropy Alloys Strengthened by Hard Intermetallic Phases, *Acta Mater.*, 2016, **116**, p 332-342.

54. Y. Guo, L. Liu, Y. Zhang, J. Qi, B. Wang, Z. Zhao, J. Shang, and J. Xiang, A Superfine Eutectic Microstructure and the Mechanical Properties of CoCrFeNiMox High-Entropy Alloys, *J. Mater. Res.*, 2018, **33**(19), p 3258-3265. https://doi.org/10.1557/JMR.2018.177

55. Y. Liu, Y. Xie, S. Cui, Y. Yi, X. Xing, X. Wang, and W. Li, Effect of Mo Element on the Mechanical Properties and Tribological Responses of CoCrFeNiMox High-Entropy Alloys, *Metals (Basel)*, 2021, **11**(3), p 486. https://doi.org/10.3390/MET11030486

56. M. Zhang, D. Wang, L. He, X. Ye, W. Ouyang, Z. Xu, W. Zhang, and X. Zhou, Microstructure and Elevated Temperature Wear Behavior of Laser-Cladded AlCrFeMnNi High-Entropy Alloy Coating, *Opt. Laser Technol.*, 2022, **149**, p 107845.

57. C.C. Yen, H.N. Lu, M.H. Tsai, B.W. Wu, Y.C. Lo, C.C. Wang, S.Y. Chang, and S.K. Yen, Corrosion Mechanism of Annealed Equiatomic AlCoCrFeNi Tri-Phase High-Entropy Alloy in 0.5 M H2SO4 Aerated Aqueous Solution, *Corros. Sci.*, 2019, **157**, p 462-471.

58. S.N. Karlsdottir, I. Csaki, I.V. Antoniac, C.A. Manea, R. Stefanoiu, F. Magnus, and F. Miculescu, Corrosion Behavior of AlCrFeNiMn High Entropy Alloy in a Geothermal Environment, *Geothermics*, 2019, **81**, p 32-38.

59. K. Masemola, P. Popoola, and N. Malatji, The Effect of Annealing Temperature on the Microstructure, Mechanical and Electrochemical Properties of Arc-Melted AlCrFeMnNi Equi-Atomic High Entropy Alloy, *J. Mater. Res. Technol.*, 2020, **9**(3), p 5241-5251.

60. A. Munitz, L. Meshi, and M.J. Kaufman, Heat Treatments' Effects on the Microstructure and Mechanical Properties of an Equiatomic Al-Cr-Fe-Mn-Ni High Entropy Alloy, *Mater. Sci. Eng. A*, 2017, **689**, p 384-394.

61. M. Löbel, T. Lindner, S. Clauß, R. Pippig, D. Dietrich, and T. Lampke, Microstructure and Wear Behavior of the High-Velocity-Oxygen-Fuel Sprayed and Spark Plasma Sintered High-Entropy Alloy AlCrFeCoNi, *Adv. Eng. Mater.*, 2021, **23**(4), p 2001253. https://doi.org/10.1002/ADEM.202001253

62. A. Anupam, R.S. Kottada, S. Kashyap, A. Meghwal, B.S. Murty, C.C. Berndt, and A.S.M. Ang, Understanding the Microstructural Evolution of High Entropy Alloy Coatings Manufactured by Atmospheric Plasma Spray Processing, *Appl. Surf. Sci.*, 2020, **505**, p 144117.

63. A.S.M. Ang, C.C. Berndt, M.L. Sesso, A. Anupam, and P. S, R.S. Kottada, and B.S. Murty, Plasma-Sprayed High Entropy Alloys: Microstructure and Properties of AlCoCrFeNi and MnCoCrFeNi, *Metall. Mater. Trans. A*, 2015, **46**(2), p 791-800. https://doi.org/10.1007/s11661-014-2644-z

64. P. Shi, Y. Yu, N. Xiong, M. Liu, Z. Qiao, G. Yi, Q. Yao, G. Zhao, E. Xie, and Q. Wang, Microstructure and Tribological Behavior of a Novel Atmospheric Plasma Sprayed AlCoCrFeNi High Entropy Alloy Matrix Self-Lubricating Composite Coatings, *Tribol. Int.*, 2020, **151**, p 106470.

65. L. Wang, F. Zhang, S. Yan, G. Yu, J. Chen, J. He, and F. Yin, Microstructure Evolution and Mechanical Properties of Atmosphere Plasma Sprayed AlCoCrFeNi High-Entropy Alloy Coatings under Post-Annealing, *J. Alloys Compd.*, 2021, **872**, p 159607.

66. A. Meghwal, A. Anupam, V. Luzin, C. Schulz, C. Hall, B.S. Murty, R.S. Kottada, C.C. Berndt, and A.S.M. Ang, Multiscale Mechanical Performance and Corrosion Behaviour of Plasma Sprayed AlCoCrFeNi High-Entropy Alloy Coatings, *J. Alloys Compd.*, 2021, **854**, p 157140.

67. W. Guo, N. Ding, G. Liu, C. Jing, H. Xu, L. Liu, N. Xu, X. Wu, J. He, and F. Zaïri, Microstructure Evolution of a Multi-Track AlCoCrFeNi High Entropy Alloy Coating Fabricated by Laser Cladding, *Mater. Charact.*, 2022, **184**, p 111660.

68. X. Li, Y. Feng, B. Liu, D. Yi, X. Yang, W. Zhang, G. Chen, Y. Liu and, P. Bai, Influence of NbC Particles on Microstructure and Mechanical Properties of AlCoCrFeNi High-Entropy Alloy Coatings Prepared by Laser Cladding, *J. Alloys Compd.*, 2019, **788**, p 485-494.

69. H. Jiang, K. Han, D. Li, and Z. Cao, Synthesis and Characterization of AlCoCrFeNiNbx High-Entropy Alloy Coatings by Laser Cladding, *Cryst. (Basel)*, 2019, **9**(1), p 56. https://doi.org/10.3390/CRYST9010056

70. H. Liu, J. Liu, P. Chen, and H. Yang, Microstructure and High Temperature Wear Behaviour of In-Situ TiC Reinforced AlCoCrFeNi-Based High-Entropy Alloy Composite Coatings Fabricated by Laser Cladding, *Opt. Laser Technol.*, 2019, **118**, p 140-150.

71. A. Munitz, S. Salhov, S. Hayun, and N. Frage, Heat Treatment Impacts the Micro-Structure and Mechanical Properties of AlCoCrFeNi High Entropy Alloy, *J. Alloys Compd.*, 2016, **683**, p 221-230.

72. C. Li, J.C. Li, M. Zhao, and Q. Jiang, Effect of Aluminum Contents on Microstructure and Properties of AlxCoCrFeNi Alloys, *J. Alloys Compd.*, 2010, **504**(SUPPL. 1), p S515-S518.

73. M. Sankar, V.V. Satya Prasad, R.G. Baligidad, and A.A. Gokhale, Effect of Vacuum Arc Remelting and Processing Parameters on Structure and Properties of High Purity Niobium, *Int. J. Refract. Metals Hard Mater.*, 2015, **50**, p 120-125.

74. D.M. Goodarzi, J. Pekkarinen, and A. Salminen, Effect of Process Parameters in Laser Cladding on Substrate Melted Areas and the Substrate Melted Shape, *J. Laser Appl.*, 2015, **27**(S2), p S29201.

75. N.I. Kourov, V.G. Pushin, A.V. Korolev, Y.V. Knyazev, M.V. Ivchenko, and Y.M. Ustyugov, Peculiar Features of Physical Properties of the Rapid Quenched AlCrFeCoNiCu High-Entropy Alloy, *J. Alloys Compd.*, 2015, **636**, p 304-309.

76. R. Vilar, Laser Cladding, *J. Laser Appl.*, 1999, **11**(2), p 64. https://doi.org/10.2351/1.521888

77. G.Y. Koga, R. Schulz, S. Savoie, A.R.C. Nascimento, Y. Drolet, C. Bolfarini, C.S. Kiminami, and W.J. Botta, Microstructure and Wear Behavior of Fe-Based Amorphous HVOF Coatings Produced from Commercial Precursors, *Surf. Coat. Technol.*, 2017, **309**, p 938-944.

78. B.S. Murty, J.W. Yeh, and S. Ranganathan, High-Entropy Alloys: Basic Concepts, *High Entropy Alloys*, in B.S. Murty, J.W. Yeh, and S. Ranganathan (eds.), (Boston), Butterworth-Heinemann, 2014, pp. 13-35, doi:https://doi.org/10.1016/B978-0-12-800251-3.00002-X

79. M.H. Tsai, J.H. Li, A.C. Fan, and P.H. Tsai, Incorrect Predictions of Simple Solid Solution High Entropy Alloys: Cause and Possible Solution, *Scr. Mater.*, 2017, **127**, p 6-9.

80. A. Takeuchi and A. Inoue, Mixing Enthalpy of Liquid Phase Calculated by Miedema's Scheme and Approximated with Sub-Regular Solution Model for Assessing Forming Ability of Amorphous and Glassy Alloys, *Intermet. (Barking)*, 2010, **18**(9), p 1779-1789.

81. M.H. Tsai, K.C. Chang, J.H. Li, R.C. Tsai, and A.H. Cheng, A Second Criterion for Sigma Phase Formation in High-Entropy Alloys, *Mater. Res. Lett.*, 2016, **4**(2), p 90-95.

82. N.D. Stepanov, D.G. Shaysultanov, G.A. Salishchev, M.A. Tikhonovsky, E.E. Oleynik, A.S. Tortika, and O.N. Senkov, Effect of V Content on Microstructure and Mechanical Properties of the CoCrFeMnNiVx High Entropy Alloys, *J. Alloys Compd.*, 2015, **628**, p 170-185.

83. C.W. Lin, M.H. Tsai, C.W. Tsai, J.W. Yeh, and S.K. Chen, Microstructure and Aging Behaviour of Al5Cr32Fe35Ni22Ti6 High Entropy Alloy, Taylor & Francis, 2015, **31**(10), pp. 1165-1170, doi:https://doi.org/10.1179/1743284715Y.0000000025

84. M.H. Tsai, K.Y. Tsai, C.W. Tsai, C. Lee, C.C. Juan, and J.W. Yeh, Criterion for Sigma Phase Formation in Cr- and V-Containing High-Entropy Alloys, *Mater. Res. Lett.*, 2013, **1**(4), p 207-212.

85. Z. Niu, Y. Wang, C. Geng, J. Xu, and Y. Wang, Microstructural Evolution, Mechanical and Corrosion Behaviors of as-Annealed CoCrFeNiMox (x = 0, 0.2, 0.5, 0.8, 1) High Entropy Alloys, *J. Alloys Compd.*, 2020, **820**, p 153273.

86. Z. Tang, M.C. Gao, H. Diao, T. Yang, J. Liu, T. Zuo, Y.Y. Zhang, Z. Lu, Y. Cheng, Y.Y. Zhang, K.A. Dahmen, P.K. Liaw, and T. Egami, Aluminum Alloying Effects on Lattice Types, Microstructures, and Mechanical Behavior of High-Entropy Alloys Systems, *JOM*, 2013, **65**(12), p 1848-1858. https://doi.org/10.1007/s11837-013-0776-z